Int J Impact Engng Vol 12, No. 2, pp 209–226, 1992
Printed in Great Britain

0734-743X 92 \$5.00 + 0.00

EFFECT OF CONSTITUTIVE MODELS ON STEADY STATE AXISYMMETRIC DEFORMATIONS OF THERMOELASTIC–VISCOPLASTIC TARGETS

R. C. BATRA and R. JAYACHANDRAN

Department of Mechanical and Aerospace Engineering and Engineering Mechanics, University of Missouri-Rolla, Rolla, MO 65401-0249, U.S.A.

(*Received* 20 *October* 1991, *and in revised form* 20 *December* 1991)

Summary We study the steady state axisymmetric deformations of a thick target being penetrated by a rigid cylindrical penetrator with a hemispherical nose and use three different constitutive relations, namely, the Litonski–Batra flow rule, the Bodner–Partom flow rule, and the Brown–Kim–Anand flow rule, to model the thermoelastic–viscoplastic response of the target. Each of these constitutive relations uses an internal variable to account for the microstructural changes in the body. The three flow rules are calibrated to give virtually identical effective stress–logarithmic strain curves during the overall adiabatic plane strain compression of a block of the target material deformed at an average strain rate of $3300\,s^{-1}$. It is found that the three constitutive relations give nearly the same value of the resisting force acting on the penetrator, temperature rise of material particles in the vicinity of the target–penetrator interface, and other macroscopic measures of deformation, such as the effective stress and logarithmic strain rate.

1. INTRODUCTION

During the penetration of a thick target by a fast moving cylindrical rod, severe deformations of the target and penetrator cause the temperature of the material particles in the vicinity of the target–penetrator interface to rise by a significant amount. Also, strain rates prevailing in this region are of the order of $10^6\,s^{-1}$. Constitutive relations that are valid over a wide range of strains, strain rates and temperatures are presently being developed by various research groups. This task is very challenging because different deformation mechanisms (for example, [1]) are active at various temperatures and strain rates, and the mechanisms themselves (e.g. thermally activated motion of dislocations, diffusion, phonon drag motion) are temperature and time dependent. Another complicating factor is the microstructural changes such as the generation/annihilation of dislocations, development of texture, dynamic recovery and recrystallization, nucleation and growth of microcracks and voids, and the development of shear bands, that occur during the plastic deformation of the material. One way to account for these microstructural changes at a macroscopic level is to use the theory of internal variables proposed by Coleman and Gurtin [2]. Chan *et al.* [3] have summarized more than 10 such constitutive relations valid for small strains. Many more are given in the review article by Inoue [4] and the book by Lubliner [5].

Here we use three constitutive relations, namely, the Litonski–Batra flow rule [6], the Bodner–Partom flow rule [7], and the Brown–Kim–Anand flow rule [8] to model the thermoelastic–viscoplastic response of the elastic–viscoplastic target. For simplicity we assume that the penetrator is rigid, and steady state as seen by an observer situated at the penetrator nose tip has been reached. Each of the aforestated three flow rules employs an internal variable to account for the microscopic deformations, and does not employ a yield surface. The material parameters in these constitutive relations have been evaluated by solving numerically an initial-boundary-value problem corresponding to the plane strain compression of a block made of the target material being deformed at an average strain rate of $3300\,s^{-1}$ and ensuring that the effective stress–logarithmic strain curves for the three constitutive relations are nearly identical. With these values of material parameters, steady state axisymmetric deformations of the target have been analysed and various quantities, such as the axial resisting force experienced by the penetrator and the pressure distribution on the penetrator nose surface, have been computed.

We note that Batra and Adam [6] conducted such a study for the Litonski–Batra and the Bodner–Partom flow rules. They evaluated the material parameters by comparing the response of the target material deformed in simple shear. With the values of material parameters so determined, they found that the Bodner–Partom law gave a very high value of the hydrostatic pressure at the target–penetrator interface as compared to that given by the Litonski–Batra flow rule. However, in the present study, all three flow rules give essentially the same value of the hydrostatic pressure and hence the axial resisting force experienced by the penetrator.

The present work is a continuation of the one initiated by Batra and Wright [9] with the goal of providing some guidelines for selecting and improving upon the previously used kinematically admissible fields in engineering models of penetration. Subsequently, Batra and co-workers [10–18] have analysed various aspects of the steady state penetration process. The reader should consult the review articles by Backman and Goldsmith [19], Wright and Frank [20], and Anderson and Bodner [21], and books by Blazynski [22], MaCauley [23] and Zukas *et al.* [24] to gain a comprehensive view of the work completed on the penetration problem. The engineering models proposed by Tate [25–28] and Alekseevskii [29] for the steady state penetration problem have been found very useful by ballisticians. Batra and Chen [30] selected a kinematically admissible field based upon the numerical studies of Batra *et al.* alluded to above, and proposed an engineering model of steady state deformations of a viscoplastic target.

2. FORMULATION OF THE PROBLEM

We use a cylindrical coordinate system with origin attached to the center of the hemispherical penetrator nose, moving with it at a uniform speed v_0, and positive z-axis pointing into the target, to describe the thermomechanical deformations of the target. We note that target deformations appear to be steady to an observer situated at the penetrator nose tip and moving with it. Equations governing the target deformations and written in the Eulerian description of motion are the following.

Balance of mass

$$\operatorname{div} \underset{\sim}{v} = 0 \tag{1}$$

Balance of linear momentum

$$\operatorname{div} \underset{\sim}{\sigma} = \rho(\underset{\sim}{v} \cdot \operatorname{grad})\underset{\sim}{v} \tag{2}$$

Balance of internal energy

$$-\operatorname{div} \underset{\sim}{q} + tr(\underset{\sim}{\sigma}\underset{\sim}{D}^{p}) = \rho(\underset{\sim}{v} \cdot \operatorname{grad})U \tag{3}$$

where

$$\underset{\sim}{D} = (\operatorname{grad} \underset{\sim}{v} + (\operatorname{grad} \underset{\sim}{v})^T)/2, \quad \underset{\sim}{W} = (\operatorname{grad} \underset{\sim}{v} - (\operatorname{grad} \underset{\sim}{v})^T)/2 \tag{4}$$

$$\underset{\sim}{q} = -k \operatorname{grad} \theta \tag{5}$$

$$U = c\theta \tag{6}$$

$$\underset{\sim}{\sigma} = -p\underset{\sim}{1} + \underset{\sim}{s} \tag{7}$$

$$\overset{\circ}{\underset{\sim}{s}} = 2G(\underset{\sim}{D} - \underset{\sim}{D}^{p}) \tag{8}$$

$$\overset{\circ}{\underset{\sim}{s}} = (\underset{\sim}{v} \cdot \operatorname{grad})\underset{\sim}{s} + \underset{\sim}{s}\underset{\sim}{W} - \underset{\sim}{W}\underset{\sim}{s} \tag{9}$$

$$\underset{\sim}{s} = 2\mu(I, \theta, \psi)\underset{\sim}{D}^{p} \tag{10}$$

$$I^2 = \tfrac{1}{2}tr(\underset{\sim}{D}^{p2}). \tag{11}$$

Here $\underset{\sim}{v}$ is the velocity of a material particle, $\underset{\sim}{\sigma}$ the Cauchy stress tensor at the present location of a material particle, ρ the mass density, $\underset{\sim}{q}$ the heat flux, $\underset{\sim}{D}$ the stretching tensor, and $\underset{\sim}{W}$ the spin tensor. Equation (5) is the Fourier law of heat conduction with k the thermal conductivity assumed here to be a constant, and θ the temperature of a material particle in °C. Equation (6) is the constitutive relation for U, and (8) for the deviatoric stress tensor $\underset{\sim}{s}$, defined by Eqn (7), where p is the hydrostatic pressure not determined by the history of the deformation, since the deformations are assumed to be isochoric. Equation (8) is Hooke's law written in the rate form, and is based on the assumption that the strain rate ($\underset{\sim}{D}$) has additive decomposition into elastic ($\underset{\sim}{D}^e$) and plastic ($\underset{\sim}{D}^p$) parts. The superimposed open circle on $\underset{\sim}{s}$ indicates its Jaumann derivative, which for steady state deformations is given by the right-hand side of (9). We recall that Pidsley [31] used the ordinary time derivative of $\underset{\sim}{s}$ in Eqn (8), which is not frame-indifferent, and equals the first term on the right hand side of (9) for steady state deformations. Equation (10) is the flow rule, and the expression for μ, wherein ψ is an internal parameter, depends upon the flow rule employed. In order to complete formulation of the problem, we need to specify the form of μ, the evolution equation for ψ, and the pertinent boundary conditions. We first give details of the three constitutive relations.

Litonski–Batra flow rule

$$2\mu(I,\theta,\psi) = \frac{\sigma_0}{\sqrt{3}I}(1+bI)^m(1-v\theta)\left(1+\frac{\psi}{\psi_0}\right)^n \tag{12.1}$$

$$\dot{\psi} = \frac{tr(\underset{\sim}{\sigma}\underset{\sim}{D}^p)}{\sigma_0\left(1+\dfrac{\psi}{\psi_0}\right)^n}. \tag{12.2}$$

Bodner–Partom flow rule

$$2\mu(I,\theta,W) = \frac{Z_2}{\sqrt{3}I\left[\dfrac{2\hat{n}}{\hat{n}+1}\ln\left(\dfrac{D_0}{I}\right)\right]^{1/2\hat{n}}} \tag{13.1}$$

$$Z_2 = Z_1 + (Z_3 - Z_1)\exp(-\hat{m}W/Z_3) \tag{13.2}$$

$$\hat{n} = \frac{\hat{a}}{T}, \quad T = 273 + \theta \tag{13.3}$$

$$\dot{W} = tr(\underset{\sim}{\sigma}\underset{\sim}{D}^p). \tag{13.4}$$

Brown–Kim–Anand flow rule

$$2\mu(I,\theta,g) = \frac{2g}{3I\xi}\sinh^{-1}(\phi^{\tilde{m}}), \tag{14.1}$$

$$\phi = \left(\frac{I}{A}\right)\exp\left(\frac{Q}{RT}\right), \quad T = 273 + \theta \tag{14.2}$$

$$\dot{g} = h_0 I\left(\max\left(0, \left(1 - \frac{g}{g^*}\right)^{\tilde{a}}\right)\right), \tag{14.3}$$

$$g^* = \tilde{g}\phi^{\tilde{n}}. \tag{14.4}$$

The constitutive relation (12), proposed by Batra [14], incorporates and generalizes that suggested by Litonski [32] for simple shearing deformations. Batra and co-workers [6,14,16] have used it to study thermomechanical penetration problems, and the initiation and growth of shear bands in viscoplastic materials. In it σ_0 is the yield stress in a quasistatic simple compression test, the material parameters b and m characterize the strain rate sensitivity of the material, v its thermal softening, and ψ_0 and n the strain hardening of the material. With ψ interpreted as the plastic strain

$$\sigma = \sigma_0\left(1+\frac{\psi}{\psi_0}\right)^n \tag{15}$$

describes the stress–strain curve in a quasistatic simple compression test. In a dynamic test, the effect of the history of deformation upon the present state of deformation is accounted for through the parameter ψ. The linear dependence of the flow stress upon the temperature rise has been used by Tate [33] in the analysis of a penetration problem, and has been observed by Bell [34], Lin and Wagoner [35] and Lindholm and Johnson [36]. Should the temperature of a material point exceed $1/v$ so as to make μ negative, we set $\mu = 0$. Thus, the material point behaves like an incompressible fluid for $\theta \geqslant 1/v$. However, the latent heat required for the phase transformation to occur is not accounted for in our work. We add that for the problem studied herein, the maximum temperature at any point in the deforming target region never reached $1/v$.

In Eqns (13.1)–(13.4), T is the absolute temperature of a material particle, the internal variable W equals the plastic work done, D_0 is the limiting value of the plastic strain rate and is usually assigned a large value, the material parameter $\hat{m}$ characterizes the rate of work hardening and $\hat{n}$ is the strain rate sensitivity parameter. In Eqn (13.2), Z_3 equals the hardening at zero inelastic strain, and Z_1 is the limit or saturation value of the work hardening of the material. We set $\hat{a}$ equal to the melting temperature of the material, and we need to specify D_0, $\hat{a}$, Z_1, Z_3 and $\hat{m}$ to characterize the material. Once T equals $\hat{a}$, we set $\mu = 0$, analogous to what we did for the Litonski–Batra flow rule. However, for problems studied herein, the temperature at a point never reached the melting temperature of the material.

In the Brown–Kim–Anand flow rule described by Eqns (14.1)–(14.4), A is called the pre-exponential factor, Q the activation energy, R the gas constant, $\tilde{m}$ the strain rate sensitivity parameter, h_0 a constant rate of athermal hardening, and g^* equals the saturation value of g associated with a given temperature/strain rate pair. Thus, g never exceeds g^*. In order to characterize the material, we need to specify ξ, $\tilde{m}$, A, Q, R, h_0, g^*, $\tilde{a}$, $\tilde{g}$ and $\tilde{n}$.

We nondimensionalize variables by scaling stress-like quantities by σ_0, length variables by r_0, time by (r_0/v_0), and the temperature by the reference temperature θ_r, defined by

$$\theta_r \equiv \frac{\sigma_0}{\rho c}. \tag{16}$$

Here r_0 equals the radius of the cylindrical part of the penetrator. Substituting for ξ from (9) into (8), and rewriting the result and Eqns (1)–(3) in terms of nondimensional variables we arrive at the following set of equations.

$$\operatorname{div} \underset{\sim}{v} = 0 \tag{17.1}$$

$$-\operatorname{grad} p + \operatorname{div} \underset{\sim}{s} = \alpha(\underset{\sim}{v} \cdot \operatorname{grad})\underset{\sim}{v} \tag{17.2}$$

$$\underset{\sim}{s} + \beta\gamma((\underset{\sim}{v} \cdot \operatorname{grad})\underset{\sim}{s} + \underset{\sim}{s}\underset{\sim}{W} - \underset{\sim}{W}\underset{\sim}{s}) = 2\beta \underset{\sim}{D} \tag{17.3}$$

$$tr(\underset{\sim}{\sigma}\underset{\sim}{D}^p) + \delta \operatorname{div}(\operatorname{grad} \theta) = (\underset{\sim}{v} \cdot \operatorname{grad})\theta \tag{17.4}$$

where

$$\alpha = \frac{\rho v_0^2}{\sigma_0}, \quad \beta = \frac{\mu v_0}{\sigma_0 r_0}, \quad \gamma = \frac{\sigma_0}{G} \text{ and } \delta = \frac{k}{\rho c v_0 r_0} \tag{18}$$

are nondimensional numbers. Henceforth we will use nondimensional variables only. Note that α, γ and δ are constants for the given problem, but β varies from point to point in the deforming region. The value of α signifies the influence of inertia forces relative to the flow stress of the material, those of γ and δ give the effect of material elasticity and the heat conduction, respectively. For most metals, γ is of the order of 10^{-3}, and it equals zero for a rigid perfectly plastic material. The value of the Weissenberg number ($\beta\gamma$) varies from 10^{-3} to 10^4 in the deforming region. For typical penetration problems involving long rod penetrators, δ is of the order of 10^{-5}; hence, the target deformations may be considered adiabatic. The form of flow rules in terms of nondimensional variables remains unaltered.

Because of our inability to solve analytically nonlinear Eqns (17), we seek their approximate solution by the finite element method. Accordingly, we consider deformations

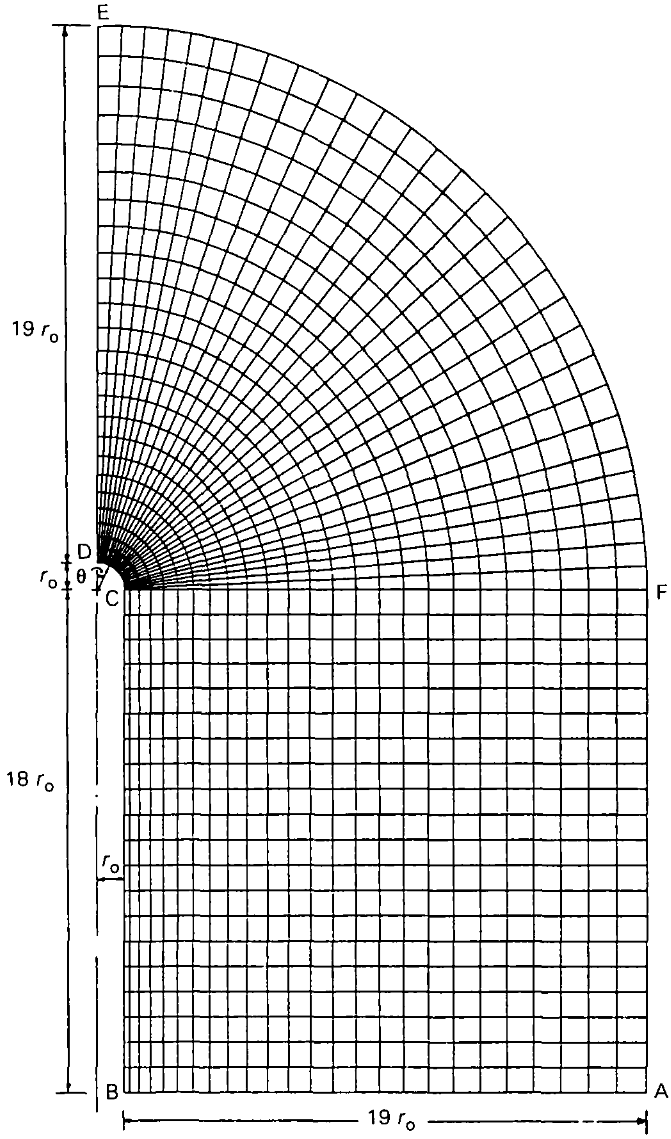

FIG. 1. The finite region studied and its discretization.

of the finite target region shown in Fig. 1 and impose on it the following boundary conditions.

$$\underset{\sim}{t}\cdot(\underset{\sim}{\sigma}\underset{\sim}{n}) = 0 \quad \text{on} \quad \Gamma_i, \tag{19.1}$$

$$\underset{\sim}{v}\cdot\underset{\sim}{n} = 0 \quad \text{on} \quad \Gamma_i, \tag{19.2}$$

$$\underset{\sim}{q}\cdot\underset{\sim}{n} = \mathrm{h_c}(\theta - \theta_a) \quad \text{on} \quad \Gamma_i, \tag{19.3}$$

$$\sigma_{zz} = 0, \quad v_r = 0, \quad \frac{\partial\theta}{\partial z} = 0 \quad \text{on the surface AB,} \tag{20.1}$$

$$v_r = 0, \quad v_z = -1, \quad \theta = 0, \quad \psi = 0, \quad g = 1, \quad p = 0, \quad s_{rr} = 0, \quad s_{\theta\theta} = 0, \quad s_{zz} = 0, \quad s_{rz} = 0 \quad \text{on the bounding surface EFA,} \tag{20.2}$$

$$\sigma_{rz} = 0, \quad v_r = 0, \quad \frac{\partial\theta}{\partial r} = 0 \quad \text{on the axis of symmetry DE.} \tag{20.3}$$

Here $\underset{\sim}{n}$ and $\underset{\sim}{t}$ are, respectively, a unit normal and a unit tangent vector to the surface, θ_a is an average temperature of the penetrator, and h_c is the heat transfer coefficient between the penetrator and the target, and Γ_i denotes the target–penetrator interface. Equation

(19.1) implies that Γ_i is smooth, and (19.2) ensures that there is no interpenetration of the target material into the penetrator and vice versa. The boundary conditions (20.3) are due to the axial symmetry of deformations. That the region R studied is adequate was established by increasing the size of the region in both r and z direction until the values of p, $\underset{\sim}{v}$, $\underset{\sim}{s}$, θ and ψ at points on Γ_i differed by less than 5%.

Figure 1 depicts the final region R so obtained, and its finite element discretization used to compute the results presented below. We note that enlarging the region ahead of the penetrator from 19 to $20r_0$ changed the value of $\|\underset{\sim}{s}\|$ by a maximum of 4.7% and of pressure, p, by 2.7%, increasing the target region behind the penetrator nose from 17 to $18r_0$ resulted in a maximum variation in $\|\underset{\sim}{s}\|$ and p of 2.2%. The values of other variables changed by considerably smaller amounts. When the target region R was divided into 700, 900 and 1250 elements proportioned as shown in Fig. 1, the peak values of the temperature rise at any node, and the pressure and the strain rate measure I at the centroid of an element were found to be (12.07, 3.42, 1.38), (12.17, 3.69, 1.52) and (12.10, 3.67, 1.53), respectively. Results presented below are for a finite element mesh with 1250 elements.

We refer the reader to [37] for details of obtaining a finite element solution of the problem.

3. NUMERICAL RESULTS

3.1. *Determination of material parameters for the three flow rules*

In order to compute predictions from the three flow rules for the penetration problem, we first need to calibrate them against the same test. Since the experimental data for a typical target material over the ranges of strain rates and temperature changes likely to occur in a penetration problem is not available in the open literature, we consider a hypothetical simple compression test. The code developed by Batra and Liu [38] to analyse the plane strain thermomechanical deformations of a viscoplastic body obeying the Litonski–Batra flow rule was modified to include the Bodner–Partom and the Brown–Kim–Anand viscoplastic models. The same initial-boundary value problem corresponding to the plane strain simple compression of a viscoplastic block being deformed at an average strain rate of $3300\,\mathrm{s}^{-1}$ was solved with each of the three flow rules. The value of each material parameter was changed in turn to assess the sensitivity of the effective deviatoric stress s_e vs strain ε_c curve. Here

$$s_e = \sqrt{\tfrac{3}{2}} tr(\underset{\sim}{s}\underset{\sim}{s}^T)^{1/2} \tag{21}$$

$$\varepsilon_c = \ln\left(\frac{l_0}{l}\right) \tag{22}$$

l and l_0 being the current and reference heights of the block. The values of material parameters determined so that the s_e vs ε_c curves for the three constitutive relations almost matched, as shown in Fig. 2, are listed below.

(a) The Litonski–Batra (LB) flow rule:

$$b = 10\,\mathrm{s}, \quad v = 1.2 \times 10^{-3}/^\circ\mathrm{C}, \quad \psi_0 = 0.1, \quad m = 0.01, \quad n = 0.13.$$

(b) The Bodner–Partom (BP) flow rule:

$$D_0 = 3.3 \times 10^6\,\mathrm{s}^{-1}, \quad \hat{a} = 1800\,\mathrm{K}, \quad Z_3 = 50\,\mathrm{MPa}, \quad Z_1 = 650\,\mathrm{MPa}, \quad \hat{m} = 0.05.$$

(c) The Brown–Kim–Anand (BKA) flow rule:

$$A = 6.346 \times 10^{15}\,\mathrm{s}^{-1}, \quad Q = 275\,\mathrm{kJ/mole}, \quad \tilde{g} = 405\,\mathrm{MPa}, \quad h_0 = 5000\,\mathrm{MPa},$$

$$\xi = 3.25, \quad \tilde{m} = 0.1, \quad \tilde{n} = 0.002, \quad \tilde{a} = 1.5.$$

Values of geometric and other material parameters that are independent of the constitutive relation employed are:

$$\rho = 7860\,\mathrm{kg/m^3}, \quad \sigma_0 = 405\,\mathrm{MPa}, \quad G = 80\,\mathrm{GPa}, \quad c = 473\,\mathrm{J/kg\,^\circ C}, \quad k = 50\,\mathrm{W/m\,^\circ C},$$

$$h = 20\,\mathrm{W/m^2\,^\circ C}, \quad \theta_a = 0, \quad r_0 = 10\,\mathrm{mm}.$$

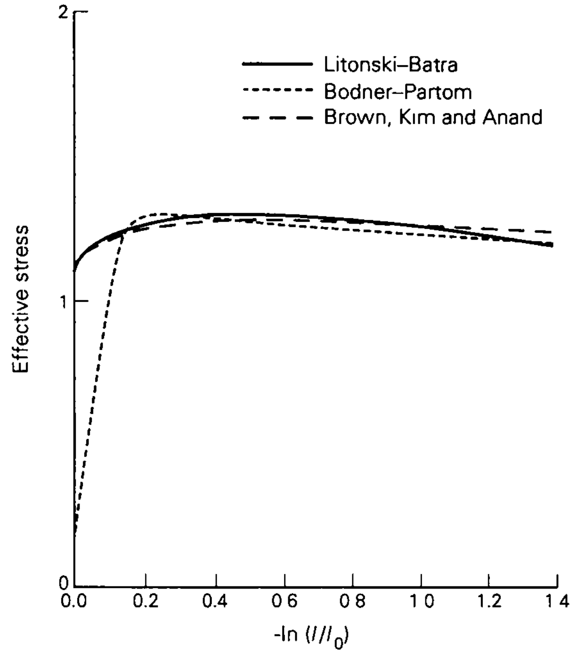

FIG. 2 The effective stress VS logarithmic strain curves for the three constitutive relations for a viscoplastic block deformed in plane strain compression at an average strain rate of $3300\,\mathrm{s}^{-1}$.

We note that the initial-boundary-value problem solved to compute the s_e vs ε_c curve is highly nonlinear, and its solution may not be unique.

The aforestated values are used in studying the penetration problem whose results are discussed below.

3.2. *Comparison of results for the penetration problem from the three constitutive relations*

Figure 3 depicts the distribution of the normal stress, temperature rise and the tangential speed on the penetrator nose surface and the strain rate measure I at the centroids of elements abutting the nose surface for $\alpha = 10$, which corresponds to the penetrator speed of 718 m/s. In these and subsequent plots, the values of various quantities have been divided by a factor so that the curves fit on the same graph. For the values of material parameters used herein, the reference temperature θ_r, used to nondimensionalize the temperature rise, equals 108.9°C. The values of the tangential speed and the strain rate measure I for the three models are nearly the same. However, the value of the normal stress and the temperature rise computed with the BP model is more than that for the other two models. The value of the temperature rise at every point on the nose surface as computed with the BKA flow rule is more than that found with the LB model, but less than that determined by using the BP flow rule. The maximum difference between the temperature rise computed at any point on the nose surface with the three flow rules is nearly 30°C for an average temperature rise there of 400°C. One reason for the temperature being essentially uniform over the nose surface is that heat is transferred mainly by convection, since the value of δ in Eqn (17.4) equals 1.9×10^{-6}. The BP flow rule gives the highest value of the normal stress on the nose surface among the three flow rules because the pressure computed with it is the highest. For example, the pressure at the stagnation point equalled 12.07 and 12.67 for the LB and the BP flow rules, respectively. The nondimensional axial resisting force experienced by the penetrator was found to be 8.19, 8.84 and 8.26 for the LB, BP and BKA flow rules, respectively.

We recall that Batra and Adam [6] used the material parameters determined by Batra and Kim [39], who evaluated them by ensuring that the computed shear stress–shear strain curve during overall adiabatic simple shearing deformations of a viscoplastic block

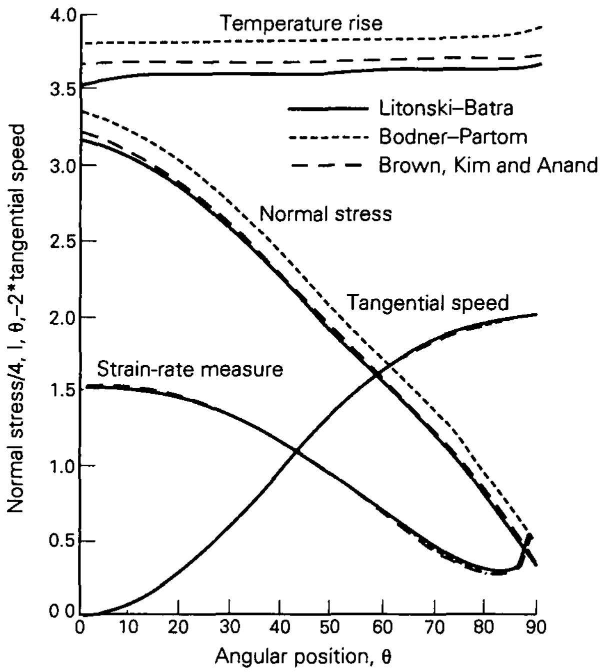

FIG. 3. Comparison of the variation of normal stress, strain rate measure, tangential speed, and the temperature rise at target particles abutting the penetrator nose surface for the three constitutive relations.

deformed at an average strain rate of $3300\,s^{-1}$ matched well with the experimental curve of Marchand and Duffy [40] for a HY-100 structural steel. Batra and Adam [6] found that for $\alpha = 4.5$, the peak pressure at or near the stagnation point equalled 18.71 and 30.16, respectively, for the LB and BP flow rules. Also, the values of the tangential speed and the strain rate measure I at points on the target–penetrator interface were not as close as that found in the present case. The BP flow rule predicted considerably higher values of the normal stress, mainly because of the significantly higher value of the hydrostatic pressure, and also of the temperature rise as compared to that for the LB flow rule. When G was set equal to infinity and material parameters assigned values used by Batra and Adam in the present code, the peak pressure with the BP flow rule was found to be twice that with the LB flow rule for $\alpha = 4.5$. We note that the target region analysed herein is more than that studied by Batra and Adam, and the problem formulation, as well as the finite element meshes used, is different.

We have plotted in Fig. 4 the variations of the axial stress $(-\sigma_{zz})$, the temperature rise θ, and the axial velocity $(-v_z)$ on the axial line, and the strain rate measure I at the centroids of elements adjoining the central line of symmetry for the three different constitutive relations studied herein. As for the distribution on the target–penetrator interface, the curves for the axial velocity and the strain rate measure are hardly distinguishable from each other for the three constitutive relations. There is not that much difference in the computed values of the temperature·rise, but the axial stress computed with the BP model differs somewhat from that computed with the other two models, primarily due to the difference in the computed values of the hydrostatic pressure. These plots reveal that, at least along the axial line, significant deformations occur at target particles situated, at most, one penetrator diameter from the target–penetrator interface. The values of (I, θ) at the stagnation point, i.e. penetrator nose tip, are found to be $(1.52, 3.53)$, $(1.52, 3.80)$ and $(1.53, 3.67)$ for the LB, BP and BKA flow rules, respectively. Since the nondimensional values of I need to be multiplied by (v_0/r_0) to get their dimensional counterparts, it is obvious that peak strain rates of the order of $1.1 \times 10^5\,s^{-1}$ occurred in the problem studied herein.

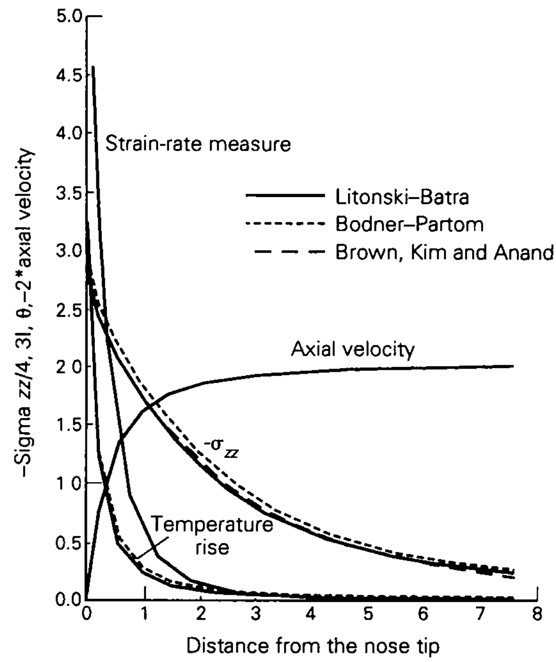

FIG. 4. Comparison of the variation of $(-\sigma_{zz})$, θ, I and $(-v_z)$ on the axial line for the three constitutive relations.

Along the axial line, uniaxial strain conditions prevail approximately. Thus, the magnitude of the deviatoric stress s_{zz} at a point on the axial line should equal 2/3 the effective flow stress defined as

$$\sigma_{\text{eff}} = 2\sqrt{3}\mu I. \tag{23}$$

The error e given by

$$e = 100\frac{|\frac{2}{3}\sigma_{\text{eff}} - |s_{zz}||}{\frac{2}{3}\sigma_{\text{eff}}} \tag{24}$$

is plotted in Fig. 5. The maximum error of 2.5% for the BP model suggests that the computed results satisfy $|s_{zz}| = 2/3\,\sigma_{\text{eff}}$ on the axial line reasonably well. The error decreases first as we move away from the stagnation point, but begins to increase at points distant $7r_0$ from the penetrator nose tip, probably because plastic deformations there are negligibly small.

An integration of the equation of motion (17.2) along the central streamline ($r = 0$) gives

$$\tfrac{1}{2}\alpha v^2 + p - s_{zz} - 2\int_0^z \frac{\partial\sigma_{rz}}{\partial r}\,\mathrm{d}z = -\sigma_{zz}(0). \tag{25}$$

Figure 6 shows the contribution from the various terms for $\alpha = 10$. The three models give nearly the same value of the kinetic energy term $(1/2\,\alpha v^2)$. The value of p for the BP model is uniformly more than that for the other two models. However, the value of s_{zz} for the three models is approximately the same. As noted by Pidsley [31] and Wright [41], there is a substantial contribution from transverse gradients of the shear stress, unlike that for a perfect fluid.

Setting $z = 0$ in Eqn (25) and comparing it with Tate's Eqn [27], we get

$$R_t = -\sigma^s_{zz} - \frac{\alpha}{2} \tag{26}$$

where R_t equals the strength parameter for the target in Tate's equation, and σ^s_{zz} is the

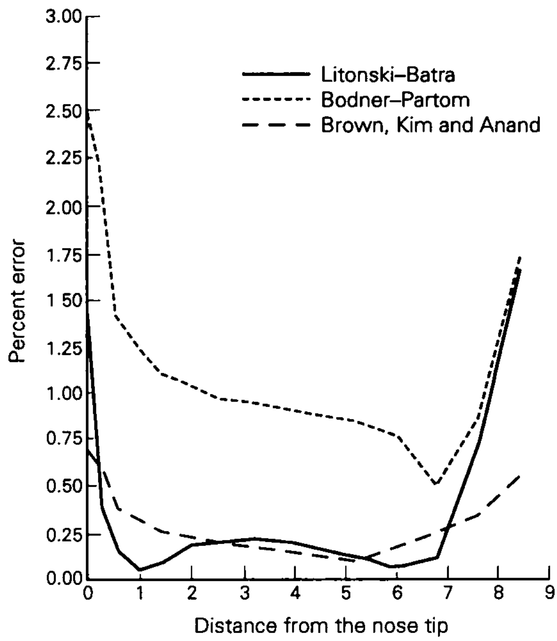

FIG. 5. Percentage error of s_{zz} in being equal to 2/3 σ_{eff} on the axial line.

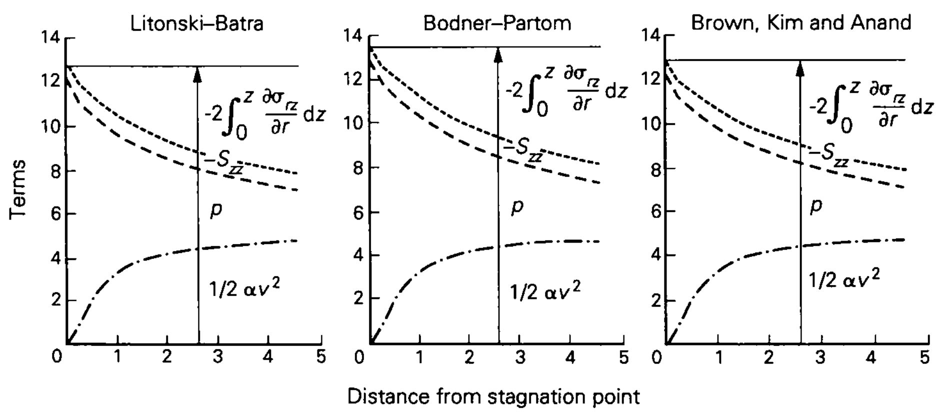

FIG. 6. Contribution of various terms in the nondimensionalized Bernoulli equation along the central stream line.

value of σ_{zz} at the stagnation point. Knowing σ_{zz}^s and α_e, we find R_t and arrive at the following

$$R_t = 8.13\ \sigma_{eff} = 7.713, \quad \text{for the LB model,} \tag{27.1}$$

$$R_t = 7.50\ \sigma_{eff} = 8.459, \quad \text{for the BP model,} \tag{27.2}$$

$$R_t = 6.57\ \sigma_{eff} = 7.886, \quad \text{for the BKA model.} \tag{27.3}$$

Tate [27] gave

$$R_t = \left[\frac{2}{3} + \ln\left(\frac{2}{3}\frac{E_t}{\sigma_0}\right)\right], \tag{28}$$

where E_t is Young's modulus for the target material. Equation (28) gives R_t equal to 6.64 for each one of the three flow rules. Thus, each one of the three models predicts a slightly higher value of R_t than that given by Tate. For an elastic perfectly plastic target, Jayachandran and Batra [10] found $R_t = 5.96$, and that its value depended weakly upon α.

We have plotted in Fig. 7 contours of the hydrostatic pressure in the deforming target

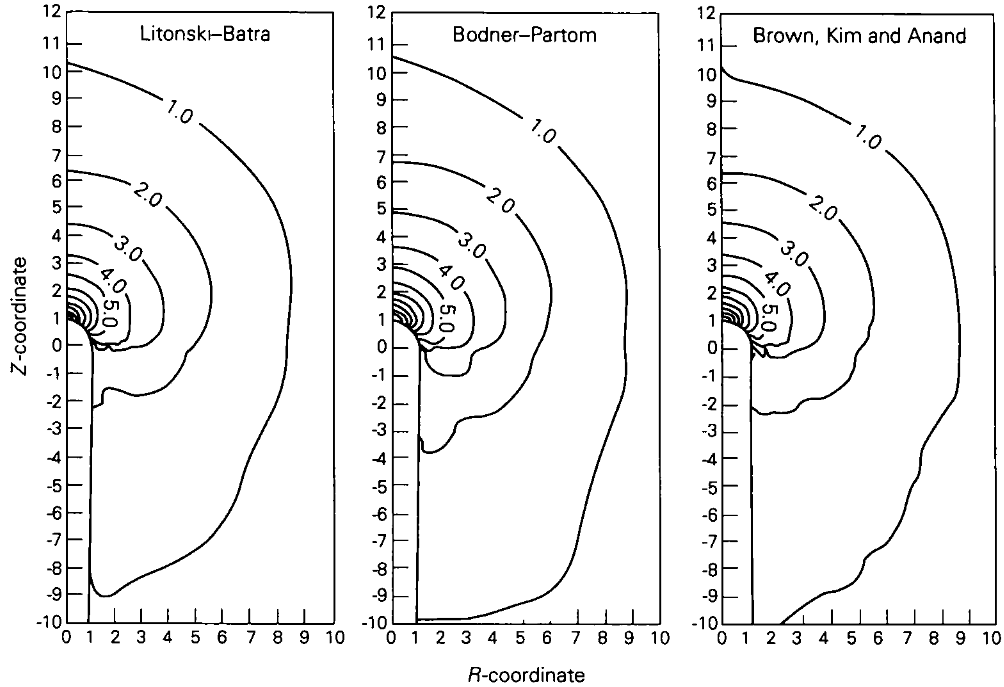

FIG. 7 Contours of the hydrostatic pressure in the deforming target region for three different flow rules.

region for the three flow rules. It is clear that along any radial line the pressure drops off more slowly for the BP model as compared to that for the other two flow rules. The contours are at an interval of 1.0 and the contour of the zero hydrostatic pressure is not plotted in order to concentrate on the region surrounding the target–penetrator interface. For each flow rule, the pressure drops off to nearly 3.0 at the nose periphery from its peak value of more than 12 at the nose tip. However, when the target material was modeled as elastic–perfectly plastic in [10], the pressure at the nose tip equalled at most 10 and dropped off to nearly 2.0 at the nose periphery. The consideration of strain-hardening, strain rate hardening, and thermal softening effects has resulted in an increase in the computed value of the hydrostatic pressure.

In the constitutive relations employed herein, it is tacitly assumed that a material point undergoes elastic and plastic deformations simultaneously. However, points on the bounding surface EFA where $\underset{\sim}{s} = \underset{\sim}{0}$ cannot be deforming plastically. Here we classify points for which the stress state satisfies the condition

$$tr(\underset{\sim}{s}^2) = \tfrac{2}{3}\sigma_{\text{eff}}^2 \tag{29}$$

as deforming plastically, and those for which the stress state lies inside the surface (29) as deforming elastically. The elastic–plastic boundary thus computed and obtained by joining points on the surface (29) by straight line segments is depicted in Fig. 8. Ahead of the penetrator nose surface, the elastic–plastic boundary extends farthest for the LB model. The distance 6.8 on the axial line of the elastic–plastic boundary for the BP and BKA models is about the same as that found when the target material is presumed to be elastic–perfectly plastic [10]. Tate [27], by using a solenoid flow model and assuming that a material point was deforming either elastically or plastically, found that the elastic–plastic boundary was located at an axial distance of 6.71, which compares well with the presently computed results.

For steady state problems, Tate [28] has proposed a method to compute the components of the finite strain tensor from a known velocity field. He found the contours of the circumferential strain to be nearly parallel to the crater surface, and the circumferential strain at a point distant r_0 from the crater tip equal to 0.05. Here we define a scalar measure

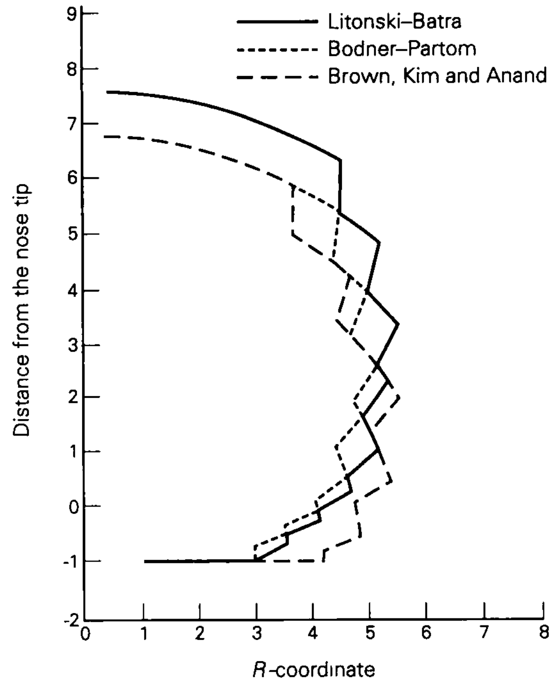

FIG. 8. Elastic–plastic boundary in the deforming target region for three different flow rules.

ε of strain by

$$\dot{\varepsilon} = \sqrt{\tfrac{2}{3}}[tr\underset{\sim}{D}^2]^{1/2} = \frac{2}{\sqrt{3}}\bar{I} \tag{30}$$

which, because of the steady state deformations, can be written as

$$(\underset{\sim}{v}\cdot \text{grad})\varepsilon = \frac{2}{\sqrt{3}}\bar{I}. \tag{31}$$

We note that ε does not equal an invariant of any finite strain tensor. We first compute $\bar{I}$ from the velocity field, and then ε as a solution of Eqn (31) with boundary condition $\varepsilon = 0$ on EFA. The contours of ε look alike for the three flow rules; those for the BP model are depicted in Fig. 9. The contours of ε are virtually parallel to the crater surface. On any radial line, ε drops off quite rapidly for a distance of r_0 from the crater surface, and then quite slowly. Comparing these contours of ε with the elastic–plastic boundary plotted in Fig. 8, one can conclude that $\varepsilon = 0.02$ on the elastic–plastic boundary. The contours of ε reveal that severe deformations of the target spread farther to the side than ahead of the penetrator nose. At points on the target–penetrator interface $\varepsilon = 3.0$. Since no failure criterion is included in our work, a material point can undergo an unlimited amount of deformation.

3.3. *Histories of field variables for target particles*

The results discussed heretofore have involved the spatial distribution of field variables. However, in order to establish testing regimes for target materials, it is useful to know the histories of stress, strain rate, temperature, etc. for a typical target particle. Accordingly, we discuss below the histories of field variables for three target particles. The results for the three models are quite similar to each other. Thus, we present results for the BKA model only; those for the LB model have been given by Lin and Batra [18]. The computer code developed by Lin and Batra has been used to first find streamlines originating from a spatial location, and then histories of field variables for that material particle. Henceforth, we identify the history of a field variable for the material particle that once occupied the place A as the history of the variable for the material particle A.

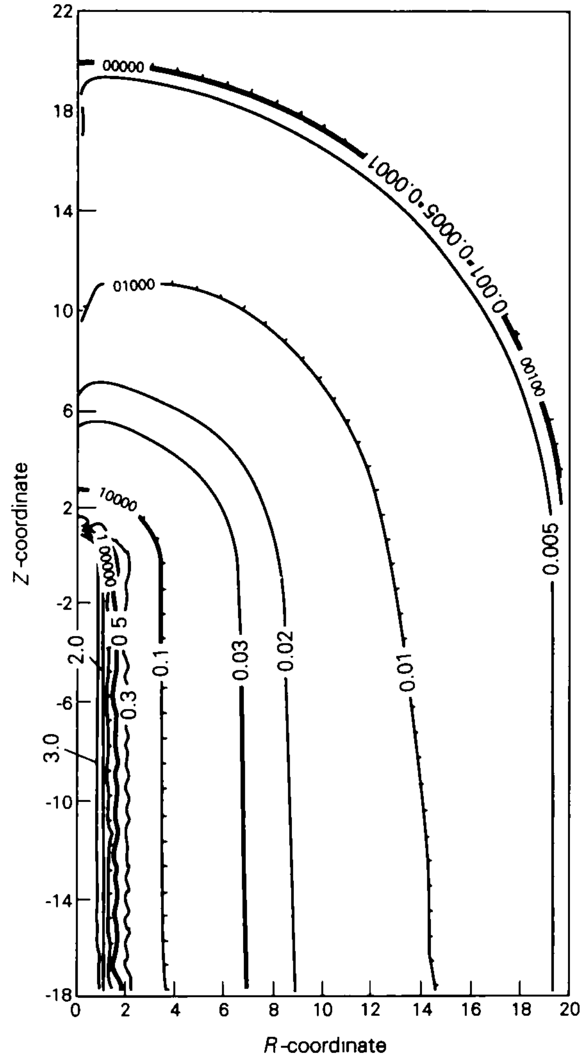

FIG. 9. Contours of strain in the deforming target region for the Bodner–Partom flow rule.

Figure 10 shows streamlines for three particles A(0.02, 8), B(0.05, 8) and C(0.1, 8). That the streamlines do not intersect should be clear from their enlarged view around the penetrator nose. Because of the different scales used along the vertical and horizontal axes, the nose shape appears flat rather than circular. The r- and z-coordinates of these three points at different times are given in Fig. 11, the time being measured from the instant these particles occupied the aforestated places. The particles reach a position near the nose tip at $t \approx 4.5$, and are near the nose periphery when $t \approx 7.25$. The time increment is computed by dividing the incremental distance a particle travels by its speed during that interval. The time history of the r- and z-components of the velocity of these three particles relative to that of the nose tip is depicted in Fig. 12. As these particles approach the penetrator nose, the r- and z-components of their absolute velocity increase. Whereas the peak values of v_r for these three particles are nearly equal, the maximum value of the z-component of the absolute velocity varies from 0.9 for particle A to 0.8 for particle C.

The time histories of the strain rate measure I and the spin are given in Fig. 13. Since the target deformations are assumed to be axisymmetric, there is only one non-zero component of spin. The small oscillations or bumps in the curves are due to numerical errors, possibly introduced because of taking larger time intervals in computing the time histories. The peak values of the spin for these three particles are nearly the same. However,

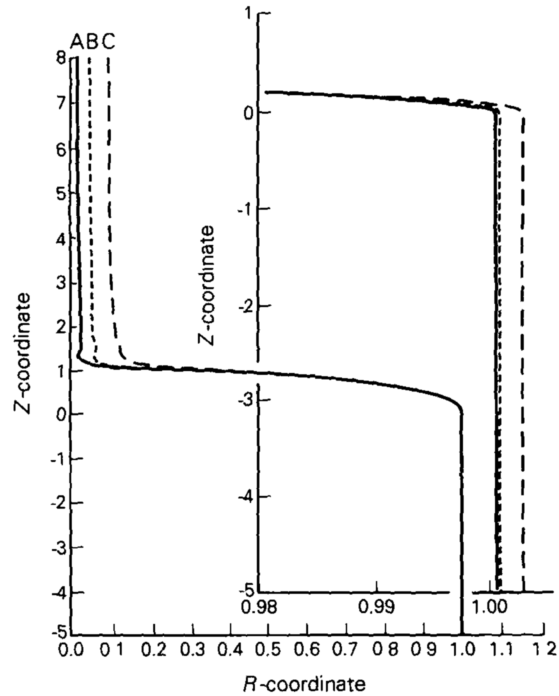

FIG. 10. Streamlines emanating from points A(0.01, 8), B(0.05, 8) and C(0.1, 8).

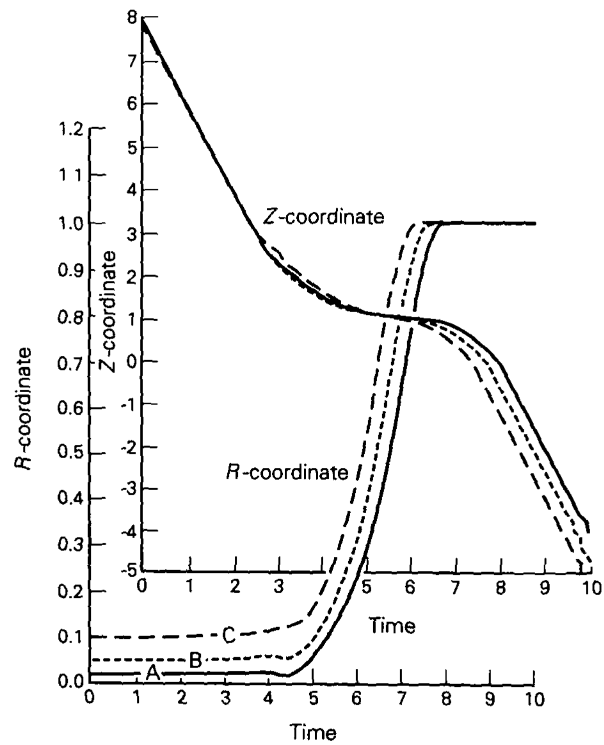

FIG. 11. The r- and z-coordinates of points A, B and C at different times.

the peak value of I for particle A is 2.1, and that for C is 1.9. For particle A, peak values of I and the spin occur when it is near the nose tip and the nose periphery, respectively. Figure 14 depicts the time histories of the temperature rise θ, hydrostatic pressure p, the internal variable g, and the effective stress σ_{eff} for these four particles. The value of g increases slowly till these particles reach near the penetrator nose tip and then stays

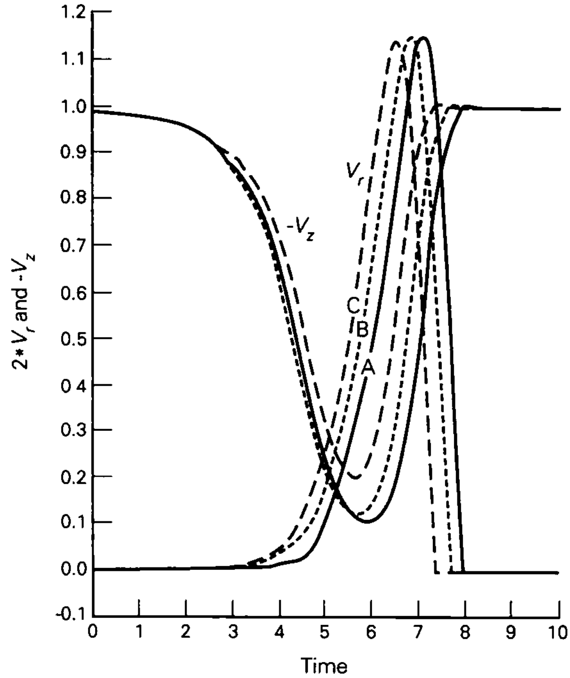

FIG. 12. The r- and z-components of the velocity of points A, B and C at different times.

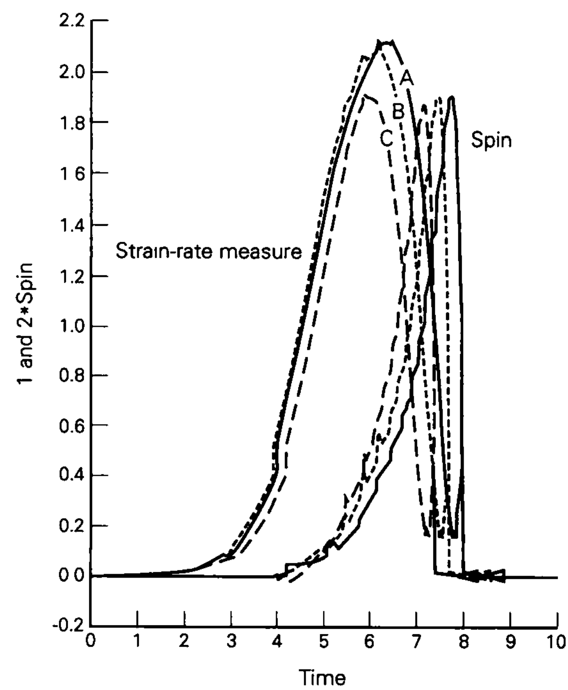

FIG. 13. Histories of the strain rate measure I and the spin for particles A, B and C.

essentially constant, suggesting that it has reached the saturation value. Nearly all of the temperature rise at a material particle occurs during the time it is going around the penetrator nose. The time histories of I, θ and σ_{eff} reveal that even though I and θ are increasing for $4 \leqslant t \leqslant 6$ for particle A, the effective stress σ_{eff} is decreasing during this time interval, implying that thermal softening exceeds the hardening caused by the strain rate and the evolution of the internal variable g. Whether or not this softening will lead to a

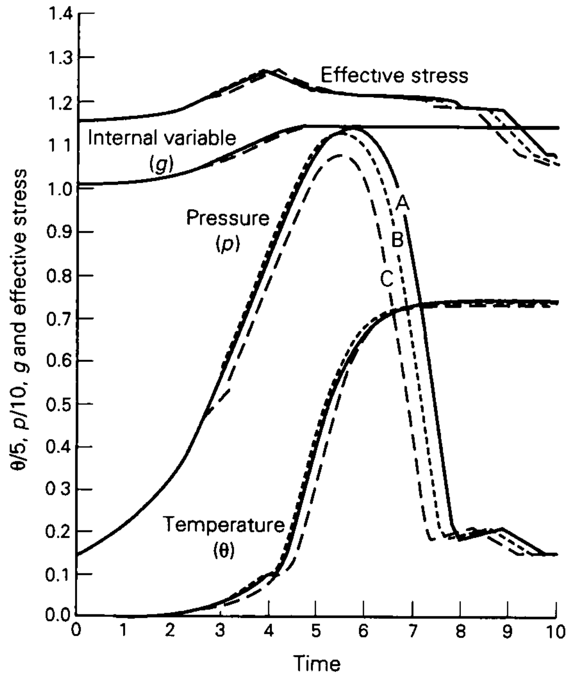

FIG. 14. Histories of the temperature rise, hydrostatic pressure, internal variable and the effective stress at points A, B and C.

material instability in the form of a shear band is unclear because of the complex state of deformations prevailing at points adjoining the target–penetrator interface.

4. CONCLUSIONS

We have analysed the steady state axisymmetric deformations of a viscoplastic target being penetrated by a rigid cylindrical hemispherical nosed penetrator. The thermomechanical response of the target material is modeled by three viscoplastic flow rules, namely, the Litonski–Batra, the Bodner–Partom and the Brown–Kim–Anand. Each of these flow rules is calibrated to give almost identical effective stress versus logarithmic strain curves for a block made of target material and deformed in plane strain compression at an average strain rate of $3300\,s^{-1}$. For the penetration problem, the BP model gives a slightly higher value of the hydrostatic pressure, and hence, normal stress on the penetrator nose surface as compared to that given by the use of the other two models. The pressure decays a little bit slowly for the BP model as one moves away from the penetrator nose surface as compared to the other two models. A comparison of the presently computed results with those obtained previously by Batra and Adam for the BP and LB models reveals that the models calibrated against a compression test give almost identical results for the penetration problem as compared to those calibrated against a simple shear test. The time histories of the field variables at three target particles initially close to the axis of symmetry suggest that they experience softening behavior, in the sense that even though the strain rate increases, the effective stress decreases. The peak values of the spin and the second invariant of the strain rate tensor are of the same order of magnitude, but a particle experiences these peak values when it is at different locations around the penetrator nose.

Acknowledgements—This work was supported by the U.S. Army Research Office Contract DAAL03-89-K-0050 to the University of Missouri, Rolla. Some of the computations were performed on the NSF sponsored supercomputer center at the University of Illinois at Urbana.

REFERENCES

1. H. J. FROST and M. F. ASHBY, *Deformation Mechanism Maps*. Pergamon Press, New York (1982).
2. B. D. COLEMAN and M. E. GURTIN, Thermodynamics with internal state variables. *J. Chem. Phys.* **47**, 597 (1967).
3. K. S. CHAN, U. S. LINDHOLM, S. R. BODNER and K. P. WALKER, A survey of unified constitutive theories. *Proceedings of 2nd Symposium on Nonlinear Constitutive Relations for High Temperature Applications*, NASA Lewis Research Center, 15–17 June, (1984).
4. T. INOUE, Inelastic constitutive relationships and applications to some thermomechanical processes involving phase transformations. In *Thermal Stresses III* (edited by R. B. HETNARSKI). North Holland, Amsterdam, pp. 192–278 (1989).
5. J. LUBLINER, *Plasticity Theory*. MacMillan Publishing Company, New York (1990).
6. R. C. BATRA and A. ADAM, Effect of viscoplastic flow rules on steady state penetration of thermoviscoplastic targets. *Int. J. Engng Sci.* **29**, 1391–1408 (1991).
7. S. R. BODNER and Y. PARTOM, Constitutive equations for elastic–viscoplastic strain-hardening materials. *J. Appl. Mech.* **42**, 385–389 (1975).
8. S. B. BROWN, K. H. KIM and L. ANAND, An internal variable constitutive model for hot working of metals. *Int. J. Plasticity* **5**, 95–130 (1989).
9. R. C. BATRA and T. W. WRIGHT, Steady state penetration of rigid perfectly plastic targets. *Int J. Engng Sci.* **24**, 41–54 (1986).
10. R. JAYACHANDRAN and R. C. BATRA, Steady state penetration of elastic perfectly plastic targets. *Acta Mechanica*, in press.
11. R. C. BATRA and T. GOBINATH, Steady state axisymmetric deformations of a thermoviscoplastic rod penetrating a thick thermoviscoplastic target. *Int. J. Impact Engng* **11**, 1–31 (1991).
12. T. GOBINATH and R. C. BATRA, A steady state axisymmetric penetration problem for rigid perfectly plastic materials. *Int. J. Engng Sci.* **29**, 1315–1331 (1991).
13. R. C. BATRA, Steady state penetration of viscoplastic targets. *Int. J. Engng Sci.* **25**, 1131–1141 (1987).
14. R. C. BATRA, Steady state penetration of thermoviscoplastic targets. *Comp. Mech.* **3**, 1–12 (1988).
15. R. C. BATRA and PEI-RONG LIN, Steady state deformations of a rigid perfectly plastic rod striking a rigid cavity. *Int. J. Engng Sci.* **26**, 183–192 (1988).
16. R. C. BATRA and P. R. LIN, Steady state axisymmetric deformations of a thermoviscoplastic rod striking a hemispherical rigid cavity. *Int. J. Impact Engng* **8**, 99–113 (1989).
17. R. C. BATRA and P. R. LIN, Histories of stress, temperature and spin in steady state deformations of a thermoviscoplastic rod striking a hemispherical rigid cavity. *Int. J. Engng Sci.* **28**, 93–98 (1990).
18. P. R. LIN and R. C. BATRA, Histories of stress, strain-rate, temperature, and spin in steady state penetration problems. *Int. J Engng Sci.* **27**, 1155–1165 (1989).
19. M. E. BACKMAN and W. GOLDSMITH, The mechanics of penetration of projectiles into targets. *Int. J. Engng Sci.* **16**, 1–99 (1978).
20. T. W. WRIGHT and K. FRANK, Approaches to penetration problems, *SMIRT Symposium*, No. 14, Impact, Lausanne, Switzerland (1987).
21. C. E. ANDERSON and S. R. BODNER, The status of ballistic impact modeling. *Int. J. Impact Engng* **7**, 9–35 (1988).
22. T. Z. BLAZYNSKI, *Materials at High Strain Rates* (edited by T. Z. BLAZYNSKI). Elsevier Applied Science, Elsevier, London (1987).
23. M. MACAULEY, *Introduction to Impact Engineering*. Chapman and Hall, London (1987).
24. J. A. ZUKAS, T. NICHOLAS, H. F. SWIFT, L. B. GRESZCZUK and D. R. CURRAN, *Impact Dynamics*. Wiley-Interscience, New York (1982).
25. A. TATE, A theory for the deceleration of long rods after impact. *J. Mech. Phys. Solids* **15**, 387–399 (1967).
26. A. TATE, Further results in the theory of long rod penetration. *J. Mech. Phys. Solids* **17**, 141–150 (1969).
27a. A. TATE, Long rod penetration models—part I. A flow field model for high speed long rod penetration. *Int. J. Mech. Sci.* **28**, 535–548 (1986).
27b. A. TATE, Long rod penetration models—part II. Extensions to the hydrodynamic theory of penetration. *Int. J. Mech. Sci.* **28**, 599–612 (1986).
28. A. TATE, A simple hydrodynamic model for the strain field produced in a target by the penetration of a high speed long rod projectile. *Int. J. Engng Sci.* **16**, 845–858 (1978).
29. V. P. ALEKSEEVSKI, Penetration of a rod into a target at high velocity, *Comb. Expl. Shock Waves* **2**, 63–66 (1966). (Translation from Russian, Faraday Press, New York.)
30. R. C. BATRA and XINGJU CHEN, An approximate analysis of steady state axisymmetric deformations of viscoplastic targets. *Int. J. Engng Sci.* **28**, 1347–1358 (1990).
31. P. H. PIDSLEY, A numerical study of long rod impact onto a large target. *J. Mech. Phys. Solids* **32**, 315–333 (1984).
32. J. LITONSKI, Plastic flow of a tube under adiabatic torsion. *Bull. Acad. Pol. Sci.* **25**, 7 (1977).
33. A. TATE, A theoretical estimate of temperature effects during rod penetration. *9th Ballistic Symposium*, pp. 2/307–2/314 (1987).
34. J. F. BELL, *Physics of Large Deformation of Crystalline Solids*. Springer-Verlag, New York (1968).
35. M. R. LIN and R. H. WAGONER, Effect of temperature, strain, and strain rate on the tensile flow stress of

I. F. steel and stainless steel type 310. *Scripta Metallurgica* **20**, 143–148 (1986).

36. U. S. LINDHOLM and G. R. JOHNSON, Strain rate effects in metals at large strain rates. In *Metal Behaviour Under High Stresses and Ultrahigh Loading Rates* (edited by V. WEISS). Plenum Press, New York, pp. 61–79 (1983).
37. R. JAYACHANDRAN and R. C. BATRA, Steady state axisymmetric deformations of a thick elastic–thermoviscoplastic target. *Int. J Engng Sci.*, in press.
38. R. C. BATRA and D. S. LIU, Adiabatic shear banding in plane strain compression problems. *J. Appl. Mech.* **56**, 527 (1989).
39. R. C. BATRA and C. H. KIM, Effect of viscoplastic flow rules on the initiation and growth of shear bands at high strain rates. *J. Mech. Phys. Solids* **38**, 859–874 (1990).
40. A. MARCHAND and J. DUFFY, An experimental study of the formation process of adiabatic shear bands in a structural steel. *J. Mech. Phys. Solids* **36**, 251 (1988).
41. T. W. WRIGHT, A survey of penetration mechanics for long rods. In *Lecture Notes in Engineering*, Vol. 3, *Computational Aspects of Penetration Mechanics* (edited by J. CHANDRA and J. FLAHERTY). Springer-Verlag, New York (1983).